J Electroceram (2012) 28:53–61
DOI 10.1007/s10832-011-9677-0

Characterization of dielectric and acoustic properties of CSD PZT thin films at high frequencies

D. Min · N. Hoivik · U. Hanke

Received: 6 October 2011 / Accepted: 25 December 2011 / Published online: 10 January 2012
© Springer Science+Business Media, LLC 2012

Abstract In this study, the microwave dielectric and the acoustic properties of $Pb(Zr_x,Ti_{1-x})O_3$ (PZT) thin films deposited using chemical solution deposition (CSD) were investigated using the same measurement setup. High dielectric constants in the range of ~280–540 and loss tangents less than 0.1 at 4 GHz were measured, where the value depends on the thickness of the PZT film. The voltage tunability of the 340 nm and 440 nm thick PZT thin films was ~34% and 5% for the 140 nm thick PZT film at 120 kV/cm and 4 GHz. The acoustic parameters of the PZT thin films under DC bias voltages were determined using a one-dimensional acoustic wave resonator model. For the PZT films of thicknesses 340 nm and 440 nm, the acoustic resonance frequency shift was about 15 MHz and the electromechanical coupling coefficient was ~10% at an electric field of 160 kV/cm. The large dielectric constant and high tunability suggest that the characterized PZT thin films may be suitable for radio frequency (RF) applications such as high-density RF MIM capacitors and other tunable devices.

Keywords PZT · Dielectric properties · Acoustic properties · MIM capacitor · RF technology

1 Introduction

Recently, the excellent piezoelectric properties of $Pb(Zr_x, Ti_{1-x})O_3$ (PZT) thin films were applied to a piezoelectrically actuated radio frequency (RF) microelectromechanical system (MEMS) switch and a thin film bulk acoustic resonator (TFBAR) [1, 2]. As a result of their large dielectric constant properties, PZT thin films can also be used for metal–insulator–metal (MIM) capacitors employed in monolithic microwave integrated circuits (MMICs) [3]. However, PZT typically suffers from a large dielectric relaxation and loss in the microwave frequency range as a result of the acoustic shear wave emission induced by the movement of the domain walls [4]. The dielectric properties of PZT thin films differ significantly from those of their bulk PZT counterparts, suggesting a dependence on the thickness of the films [4, 5]. Although several researchers have reported the piezoelectric and dielectric properties of PZT thin films [6, 7] and their dependence on the film thickness [8, 9], there remains a lack of data relating the effect of film thickness on the dielectric properties in the gigahertz frequency range. In this work, we have determined the microwave dielectric properties of PZT thin films, as well as their voltage tunability over different thicknesses. The test structure for characterization was modeled on a MIM capacitor, in which the electric field was ideally located perpendicular to the dielectric layer. However, because of the large parasitic effects occurring during the microwave measurement, it was difficult to directly obtain the microwave dielectric properties from a simple parallel plate capacitor. Several techniques were suggested for the characterization of dielectric thin films using the MIM capacitor [10, 11]. Among the suggested techniques, the microwave measurement technique proposed by Ma et al. [12] has been successfully employed for thin films with high and low dielectric constants, and continues to be improved [13, 14]. The unwanted parasitic effect, induced by the outer ground electrode (G) shown in Fig. 3(a), was effectively removed using two test structures with different sized annular ring slots, while maintaining the same outer radius for the top metal layer. The acoustic properties of the PZT thin films were derived from the same measurement setup as the dielectric property measurement. PZT films

D. Min (✉) · N. Hoivik · U. Hanke
Vestfold University College,
Institute of Micro and Nano Systems Technology,
3103 Tønsberg, Norway
e-mail: Deokki.Min@hive.no

are known to be a potential candidate for broadband filter applications because of their high electromechanical coupling coefficient [2]. We have simulated the effects of the acoustic resonance responses induced by the DC electric field dependent piezoelectric and electrostrictive properties using a one-dimensional (1-D) electro-acoustic model of the multilayer capacitor structure.

2 Experimental procedure

Test wafers were prepared by the following method. A SiO_2 thermal layer with a thickness of 540 nm was deposited on a high resistivity Si wafer (~10 kΩ cm) with a thickness of 720 μm. Using sputtering, Ti and Pt layers were sequentially added on the SiO_2 layer, with thicknesses measuring 15 nm and 220 nm, respectively. Chemical solution deposition (CSD) was used to deposit PZT layers of various thicknesses (140 nm, 340 nm, and 440 nm) on the Pt layer. Details of the PZT deposition process were previously reported in [15]. A 720 nm thick Au top metallic layer was deposited on a 15 nm thick Cr adhesive layer using DC magnetron sputtering. Standard lithography and wet etching processes were carried out to pattern circular electrodes on top of the Au/Cr layer. The thicknesses of the films were measured using a focused ion beam (FIB, SMI3050TB) technique. The cross sectional view of a test wafer fabricated using FIB milling is shown in Fig. 1. Figure 2 shows the X-ray diffraction $\theta/2\theta$ spectra of the MIM capacitor with the thickest PZT film (440 nm). The PZT film is clearly crystallized with the (001) and (110) orientations dominating.

The top electrode in the capacitor was designed so the inner circular electrodes would have an inner radius of 20 μm or 45 μm and an outer radius of 75 μm. Figure 3 shows a top and cross sectional schematic view of the MIM capacitor. An Agilent E8364B vector network analyzer (VNA) and a ground-signal-ground (GSG) Cascade Microtech infinity probe with a pitch of 200 μm were used for the microwave characterization of all the samples. An on-wafer calibration routine using a calibration substrate provided by the probe manufacturer was carried out before performing measurements. In order to characterize the electric field induced dielectric properties, an E5270 DC analyzer (Agilent Technologies) was connected to the network analyzer so that a DC bias could be applied to the MIM capacitor through the RF probe. All the samples in our experiments for the microwave characterization were measured at room temperature, and the poling process was not carried out so

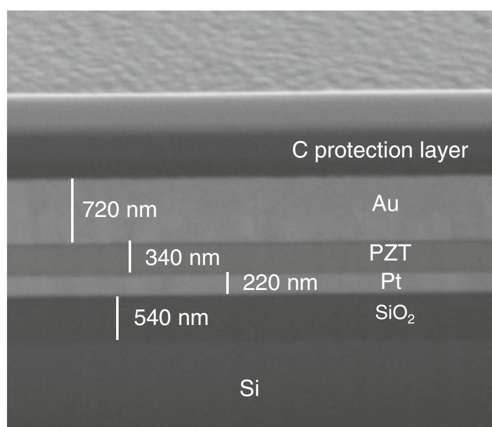

Fig. 1 FIB image (cross sectional view) of a test wafer which specifically shows the 720 nm Au layer and the 340 nm PZT thin film, which is deposited on to the $Pt/Ti/SiO_2/Si$ substrates. The Cr and Ti layers were so thin that the layers were not labeled

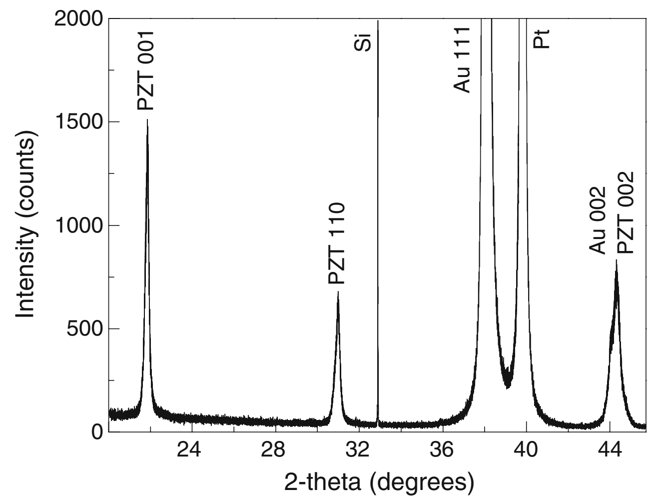

Fig. 2 X-ray diffraction $\theta/2\theta$ (°) scan of the 440 nm thick PZT films on $Pt/Ti/SiO_2/Si$ substrates

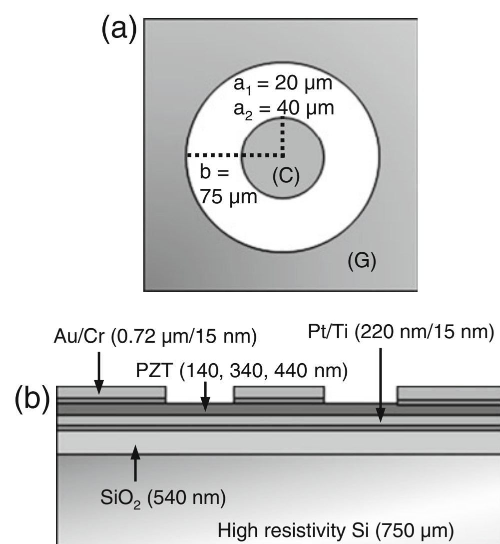

Fig. 3 Schematic of top (**a**) and cross-sectional view (**b**) of the MIM capacitor structure

that the dielectric properties of the as-deposited films could be obtained.

3 Results and discussion

The S-parameters were recorded by performing one-port VNA measurements at room temperature; these parameters were then converted into load impedance (Z_c) as follows:

$$Z_c = Z_o \frac{1 + S_{11}}{1 - S_{11}} = R + jX \quad (1)$$

where Z_o is the characteristic impedance (50Ω), S_{11} is the measured S-parameter, and R and X are the real and imaginary parts of the impedance, respectively.

The capacitance of the simple parallel plate MIM capacitor was calculated using the following equation:

$$C = -\frac{1}{X\omega} = \frac{A\varepsilon_o\varepsilon_r}{t} \quad (2)$$

where C is the measured capacitance, and t and A are the dielectric film thickness and inner circle electrode area, respectively, ω is the angular frequency, and ε_r is the dielectric constant of the PZT thin film.

It should be noted that the MIM capacitor with an annular ring slot on the top of the metal layers cannot be modeled as a simple parallel plate capacitor without resulting in errors in the extracted parameters. Instead, it must be modeled using an equivalent circuit, as shown in Fig. 4 [14].

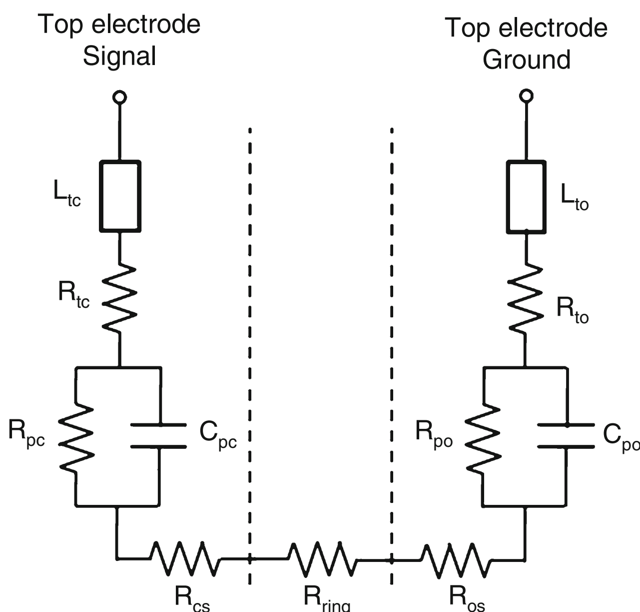

Fig. 4 Schematic showing the MIM capacitor equivalent circuit model with an annular ring slot

Results of the capacitance measurements performed using only one capacitor to determine the complex dielectric constant of a dielectric thin film may not be reliable because of the parasitic effects induced by the outer ground electrodes (G) [12]. Therefore, instead of using only one capacitor, two capacitors with different inner radii but the same outer radius were modeled, and the impedance values of the two capacitors were subtracted from each other to appropriately account for the outer ground electrode.

The complex dielectric constant consists of real part of ε_1 and imaginary part of ε_2.

The real part of the impedances after subtraction was expressed as follows:

$$R_1 - R_2 = (R_s/2\pi)\ln(a_2/a_1) + R_{cs1} - R_{cs2} + R_{tc1} - R_{tc2} + \frac{t\varepsilon_2}{\omega\pi\varepsilon_o\left(\varepsilon_1^2+\varepsilon_2^2\right)}\left(\frac{1}{a_1^2} - \frac{1}{a_2^2}\right) \quad (3)$$

The imaginary part of the impedances after subtraction was expressed as follows:

$$X_1 - X_2 = \frac{t\varepsilon_1}{\omega\pi\varepsilon_o\left(\varepsilon_1^2 + \varepsilon_2^2\right)}\left(\frac{1}{a_2^2} - \frac{1}{a_1^2}\right) + \omega(L_{tc1} - L_{tc2}) \quad (4)$$

where a_1 and a_2 are the different radii of the inner circle electrodes, R_s is the sheet resistance of the bottom electrode, R_{tc} and L_{tc} are the resistance and the inductance of the top circular electrode, respectively, and R_{cs} is the resistance of the bottom electrode of the inner circular capacitor (C). The resistances R_{tc} and R_{cs}, and inductance L_{tc} were calculated on the basis of the Bessel function of the first kind and zero order [12, 16].

Thus, using (3) and (4), the formula for determining the complex dielectric constant of a dielectric thin film was

$$\tan\delta = \frac{\varepsilon_2}{\varepsilon_1} = \frac{(R_s/2\pi)\ln(a_2/a_1) - R_1 + R_2 + R_{cs1} - R_{cs2} + R_{tc1} - R_{tc2}}{X_1 - X_2 - \omega(L_{tc1} - L_{tc2})} \quad (5)$$

$$\varepsilon_1 = \frac{t\left(1/a_2^2 - 1/a_1^2\right)\left((X_1 - X_2) - \omega(L_{tc1} - L_{tc2})\right)}{\omega\pi\varepsilon_o} \Big/ \left\{ \left((X_1 - X_2) - \omega(L_{tc1} - L_{tc2})\right)^2 + \left((R_s/2\pi)\ln(a_2/a_1) - R_1 + R_2 + R_{cs1} - R_{cs2} + R_{tc1} - R_{tc2} \right)^2 \right\} \quad (6)$$

During the dielectric properties measurements (dielectric loss tangent in Fig. 5(a–c) and dielectric constant in Fig. 7(a–c)), oscillations related to the acoustic resonance response were observed for all PZT thicknesses. In Fig. 5(a–c), the sharp resonance peaks depending on the thickness were associated with the DC electric field dependent piezoelectric and electrostrictive properties of the PZT thin films [17, 18] rather than dielectric relaxation [9] and RF

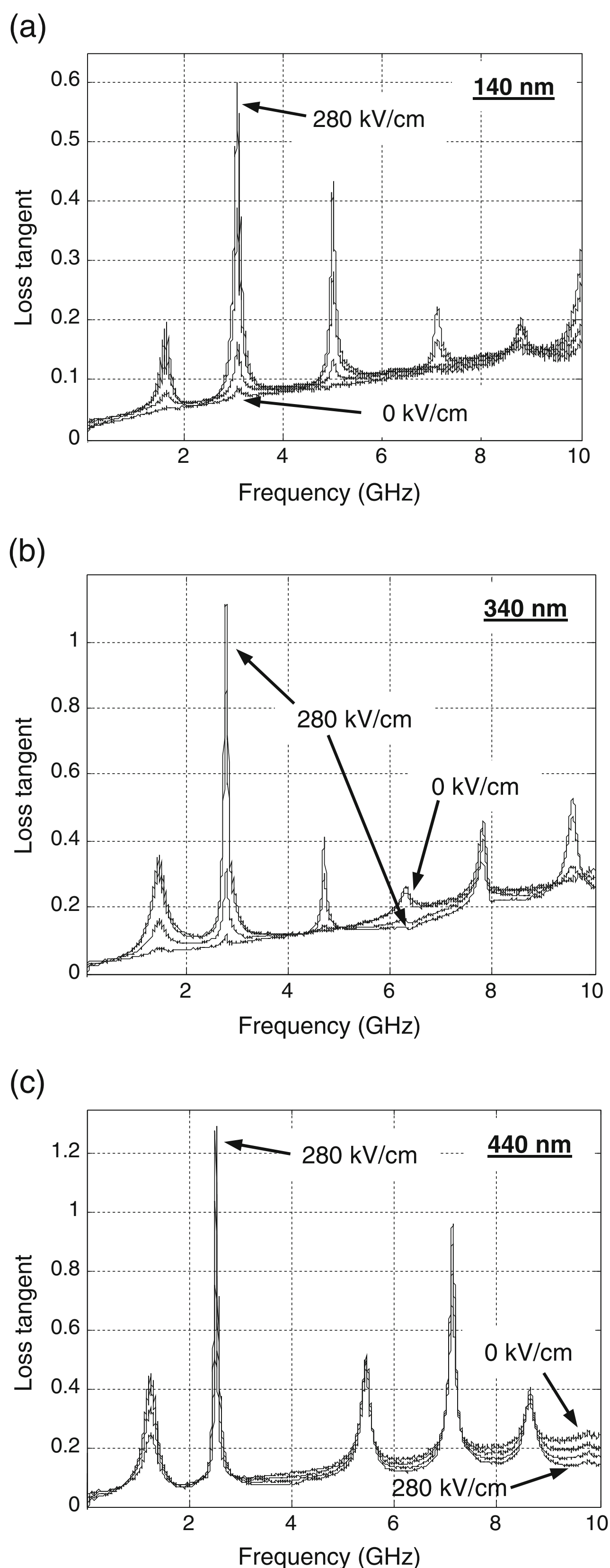

Fig. 5 Measured dielectric loss tangents (**d**, **e**, and **f**) of PZT films obtained using (5) following 40 kV/cm electric field increment changes as a function of frequency

measurement setup [19]. The electric polarization of the ferroelectric thin films increased with the DC electric field; this results in an increased piezoelectric response, followed by a resonance response [20]. In Fig. 6, different resonance frequencies (anti-resonances) are displayed and were attributed to the mechanical resonance condition of the resonating device, whose piezoelectric film thickness was inversely proportional to the resonance frequency. The resonance magnitude increases as the thickness increases, which means the piezoelectricity of the PZT thin films is thickness dependent [21]. The piezoelectric effect detected at zero electric field may be a result of the self-polarization effect found in ferroelectric thin films [18, 22]. The dielectric loss of PZT thin films increases with increasing thickness and frequency. The Butterworth Van-Dyke (BVD) equivalent circuit model for the piezoelectric resonator could be added to the MIM capacitor model in Fig. 4 in order to remove the acoustic resonance effects in the measurement results of dielectric loss tangent (Fig. 5) and dielectric constant (Fig. 7).

In order to investigate the DC electric field tunability of PZT films, different DC bias voltages were applied to the MIM capacitor structures through a RF probe. The extracted dielectric constants using (5) were plotted up to 10 GHz and are shown in Fig. 7(a–c). The tunability was strongly related to the PZT film thickness. Figure 8 shows the voltage tunability, defined as $T(V) = 1 - \varepsilon_r(V)/\varepsilon_r(0)$. The voltage tunability was ~5% for the 140 nm thick PZT film and ~34% for the 340 and 440 nm thick PZT films at 120 kV/cm and 4 GHz. The dielectric constant of the PZT films was also thickness dependent. As the PZT film thicknesses increased, the dielectric constant also increased. The presence of a thin dielectric layer with a low dielectric constant at the electrode interface may explain the relatively large difference in the dielectric

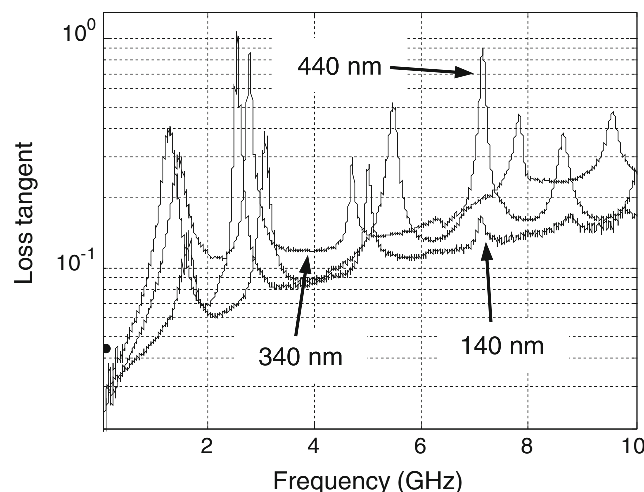

Fig. 6 Measured loss tangent values of PZT thin films at 160 kV/cm

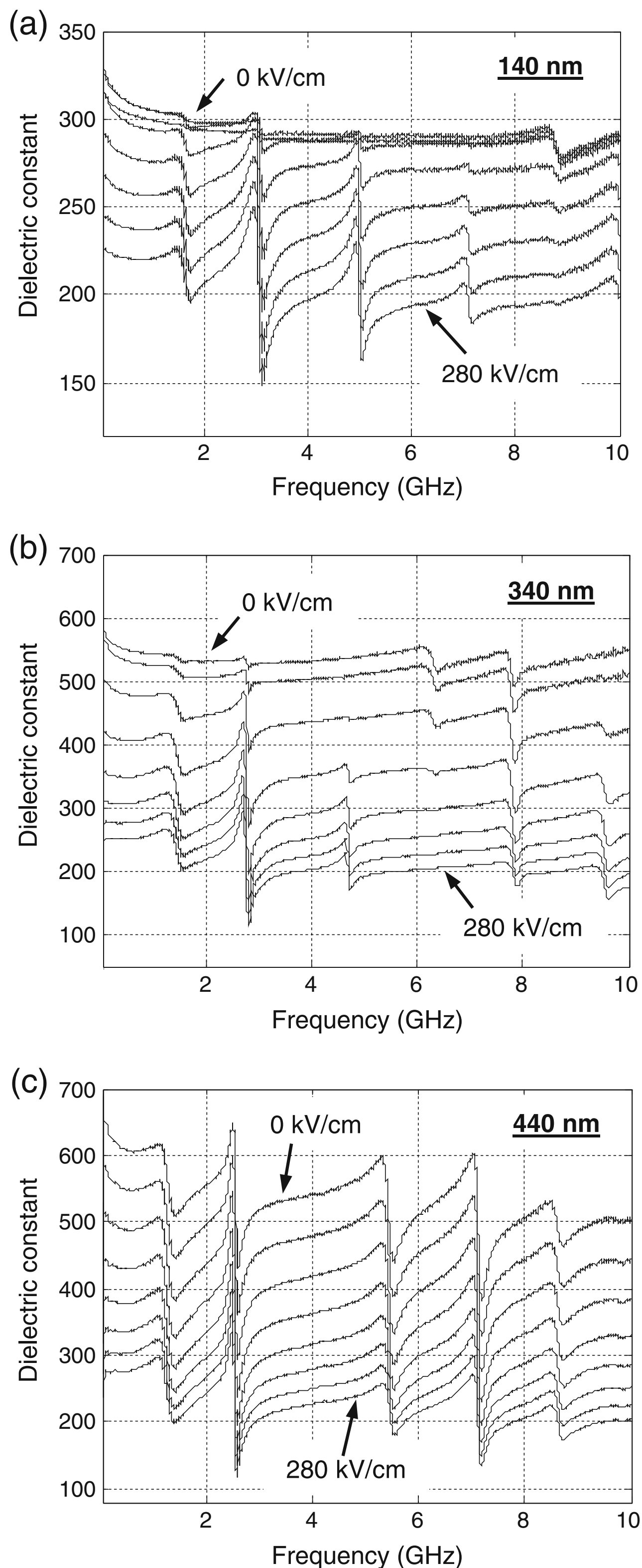

Fig. 7 Measured dielectric constants of PZT thin films of various thicknesses: (**a**) 140 nm, (**b**) 340 nm, and (**c**) 440 nm, while the electric field was increased in steps of 40 kV/cm

constant for different thicknesses of the PZT film [23]. This theory was tested using a two layer model. The

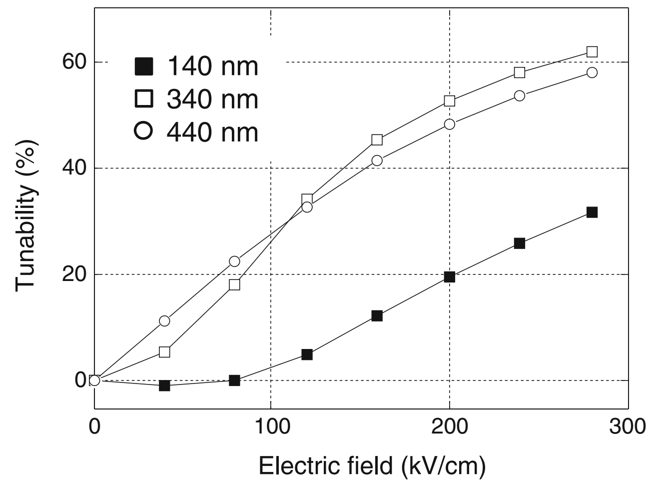

Fig. 8 Tunability of the PZT thin films versus DC electric field at 4 GHz for various PZT thin film thicknesses

PZT thin film was assumed to consist of two sublayers with different dielectric constants: one with a low and one with a high dielectric constant. Therefore, the overall capacitance of the PZT thin film was substantially decreased since the two capacitors were in series, corresponding to the sublayers. However, the effect of the thin dielectric layer decreased with increased thickness of the PZT film. Incomplete crystallization of the PZT process at the initial or last growth stage may result in a thin dielectric layer with low dielectric constant and poor quality [24]. The large variations near the resonance frequencies are attributed to the piezoelectric properties of PZT films and are not removed in the MIM capacitor model.

Figure 9 shows the extracted dielectric constant (a) and loss tangent (b) of a 440 nm thick PZT thin film as a function of frequency up to 10 GHz obtained using (5) and (6). As shown in this figure, the results obtained using (2), where only one capacitor with a 20 μm inner circle radius was used, illustrates the high frequency dependence where the effects of the impedance of the outer ground electrode area (G) become pronounced with an increase in the frequency.

PZT thin films have high electromechanical coupling coefficients, making them potential candidate for broadband filter applications [2]. The coupling coefficient increases as the applied DC bias voltage increases [25]. These features prompted an investigation of the films' acoustic properties for RF applications such as a TFBAR. The electrical impedance of the multilayer MIM capacitor structure (Fig. 3) was measured under different DC bias voltages in order to determine the acoustic properties of the PZT thin films. The multilayer structure was modeled taking into account all the layers of the electrodes and dielectrics, except the adhesive layers of Cr and Ti. The effects of these layers on the results

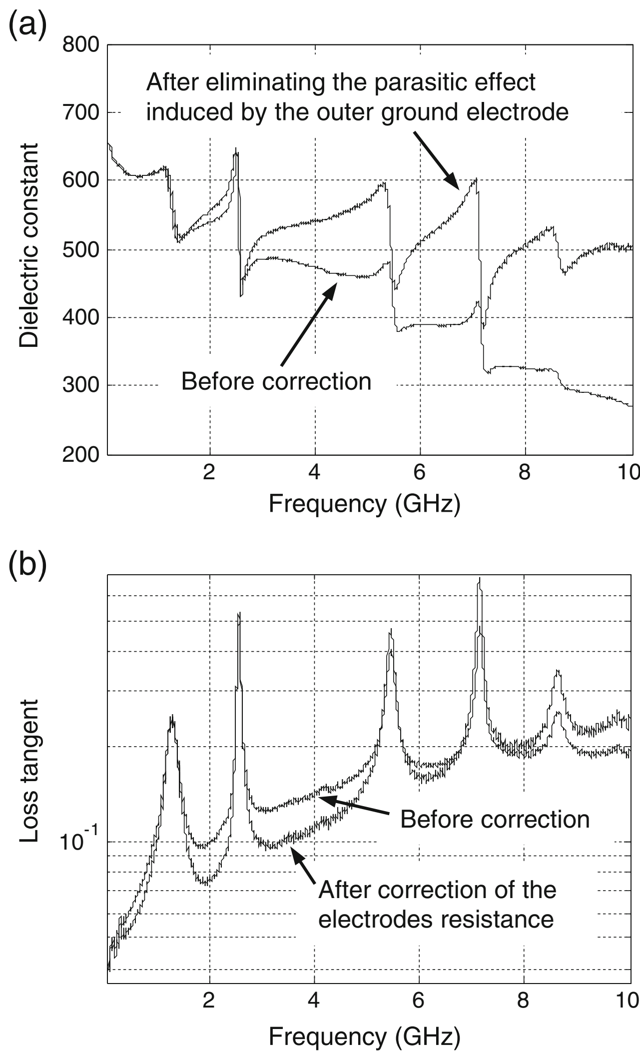

Fig. 9 Measured dielectric constant (**a**) and loss tangent (**b**) of 440 nm PZT thin film as a function of frequency

were small enough to be negligible due to the thin layers. The electrical impedance at the interfaces of the top (Au/PZT) and bottom (PZT/Pt) terminals were calculated as follows [26]:

$$Z = \frac{1}{j\omega C} \cdot \left[1 - K_t^2 \frac{\tan\varphi}{\varphi} \frac{(z_t+z_b)\cos^2\varphi + j\sin 2\varphi}{(z_t+z_b)\cos 2\varphi + j(z_t z_b + 1)\sin 2\varphi}\right] \tag{7}$$

where $\omega = 2\pi f$ is the angular frequency and C is the static capacitance, taking into account the dielectric loss of a piezoelectric layer described as

$$C = \frac{A\varepsilon_o \varepsilon_r^S}{t}(1 - j\tan\delta) \tag{8}$$

where A is the top circular electrode area and ε_r^S and tan δ are the dielectric constant under constant strain and loss tangent of the piezoelectric layer, respectively. The value t is the film thickness.

The complex acoustic phase, φ, was defined as

$$\varphi = \frac{\beta t}{2}\left(1 - \frac{j}{2Q}\right) \tag{9}$$

where β is the phase constant given by the longitudinal acoustic velocity (v_D) as follows:

$$\beta = \frac{2\pi f}{v_D} \tag{10}$$

The value Q is the acoustic quality factor of the piezoelectric layer.

The values of z_t and z_b are the acoustic impedances loading a piezoelectric layer at the top and bottom sides, respectively, obtained using the following impedance transformation [18]:

$$Z_{in} = Z_i \frac{Z_{i+1} + Z_i \tanh(\gamma_i t_i)}{Z_i + Z_{i+1}\tanh(\gamma_i t_i)} \tag{11}$$

where $y_i = a_i + j\beta_i$ is the complex propagation constant for the ith layer.

The acoustic wave propagation loss, α is given by the phase constant and quality factor as follows:

$$\alpha_i = \frac{\beta_i}{2Q_i} \tag{12}$$

The Z_{i+1} and Z_i values are the acoustic impedances of the $(i+1)$th and the ith layers, respectively. The electromechanical coupling constant for the thickness longitudinal vibration (K_t^2) is defined as

$$K_t^2 = \frac{e_{33}^2}{c_{33}^D \varepsilon_o \varepsilon_r^S (1 - j\tan\delta)} \tag{13}$$

in which c_{33}^D is the elastic stiffness coefficient of the piezoelectric layer (Pa) under constant electric displacement and e_{33} is the piezoelectric stress constant (C/m^2). The subscript 33 indicates the z direction.

Figure 10 shows the electrical impedances [real (a, c, and e) and imaginary (b, d, and f)] of the multilayer MIM capacitor structures with PZT thin films simulated using (7) and the measured impedances between 2.2 GHz and 3.5 GHz. The measured impedances were obtained for a 20 μm inner radius of the top electrode. The resonance responses were measured as the DC bias voltage was applied and increased stepwise until it reached 280 kV/cm. However, the resonance magnitude did not remain constant; instead the value decreased when the bias was repeatedly switched on and off. This decrease could be associated with PZT thin film fatigue under a high DC electric field [27]. In order to fit the simulated impedance to the measured one, the parameters v_D and e_{33} were adjusted for applied DC bias voltage. For the zero bias voltage, the Au layer thickness was changed down 0.2~6.9% so

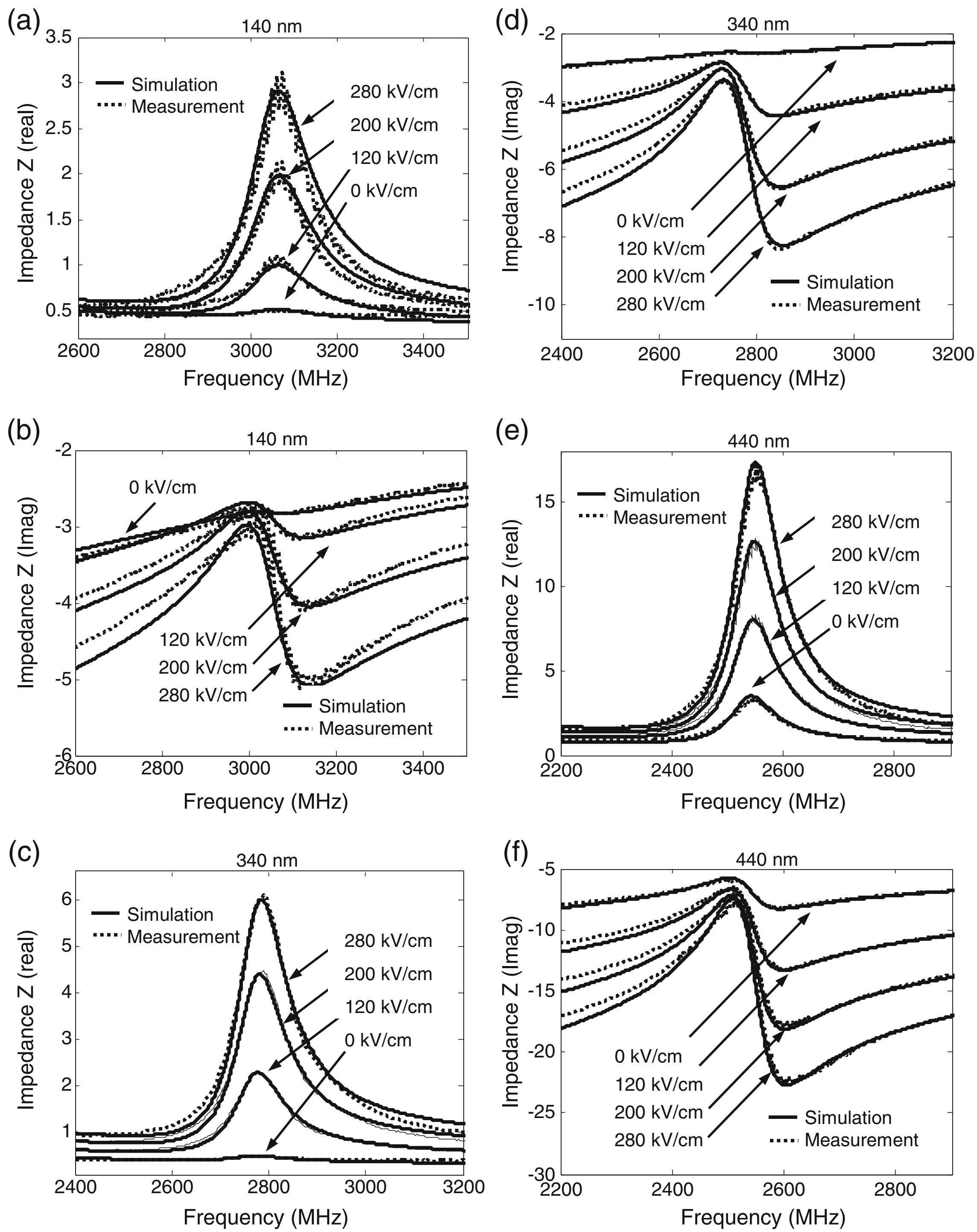

Fig. 10 Measured and simulated electrical impedances of the multilayer capacitor structure with PZT thin films as a function of the real (**a**, **c**, and **e**) and imaginary (**b**, **d**, and **f**) portions of frequency

that the acoustic velocity of the PZT thin films was set to 4,500 m/s [28]. The top Au thickness remained thicker than the piezoelectric film. Even a small change in Au thickness showed large influences on the resonance frequency. It is important to note that during the RF measurement, a RF probe was contacting the top Au surface with a pushing force, decreasing the Au thickness slightly. The acoustic parameters of the other materials used are displayed in Table 1. For non-zero bias voltages applied to the capacitor, v_D in (10) was modified to fit with the resonance frequency of the measured impedance, also referred to as the real part. Secondly, the measured

Table 1 Acoustic parameters of layers in PZT FBAR

Layer	Acoustic wave velocity (*m/s*)	Acoustic impedance *kg/(sm²)*	Acoustic Q-factor
Air	360	400	–
Au	3428	$66.1 \cdot 10^6$	50 @ 2.5 GHz
PZT	4500 [29]	$34.9 \cdot 10^6$	15 @ 2.5 GHz
Pt	3300	$69.8 \cdot 10^6$	150 [19]
SiO_2	5700	$12.5 \cdot 10^6$	500 [19]
Si	8433	$19.7 \cdot 10^6$	20 @ 2.5 GHz

dielectric constant (ε_r^S) at the resonance frequencies was inserted in (8) and (13) with e_{33} set to zero so that the simulated impedance (imaginary) fits at the maximum slope point where the first derivative is the maximum. Then, e_{33} in (13) was increased to fit with both the real and imaginary parts of the impedance. The ε_r^S and e_{33} values were minimally adjusted to obtain a better fit. The simulated impedance agreed closely with the measured impedance within the measured frequency range. The *Q*-factor of the PZT films derived was ~15 for all the measured impedances under different DC bias voltages. The measured Q-factor of the PZT thin films is lower than other PZT thin films [2], and it may be attributed to the high frequency. The Q-factor is decreased with frequency. The loss tangent was ~0.1, 0.15, and 0.15 for PZT films of thickness 140 nm, 340 nm, and 440 nm, respectively. The measured impedances (real part) of the FBAR structure with PZT thicknesses of 340 nm and 440 nm showed a positive shift in the resonance frequency as the DC bias voltage increased. The resonant frequency shifts were around 10 MHz and 15 MHz for 340 nm and 440 nm, respectively. However, for the smallest thickness of 140 nm, a resonance frequency shift was not observed.

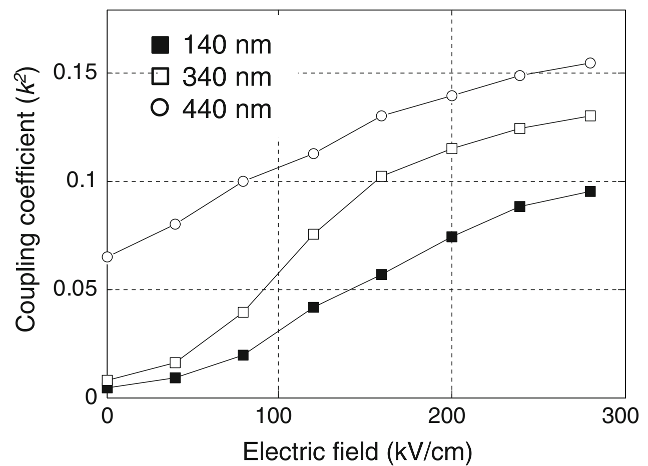

Fig. 12 Graph showing the coupling coefficient for various PZT thin film thicknesses as a function of DC electric field

The nonlinear electrostriction coefficient (*M*) of PZT films, directly related to the shift of the resonant frequency [29], was estimated by extracting the stiffness coefficient (c_{33}^D) in (14)

$$c_{33}^D = v_D^2 \rho \tag{14}$$

where ρ is the density of PZT. In the calculation, a standard density of 7,750 kg/m^3 was used.

In Fig. 11, c_{33}^D of the 440 nm thick PZT film almost linearly increases with the DC electric field. However, c_{33}^D for the 140 nm thick PZT film was constant because there was no resonant frequency shift. In particular, it was observed that the resonance frequency of the 340 nm PZT structure was shifted negatively until 80 kV/cm, and c_{33}^D decreased. This phenomenon was not clearly understood. It may be the result of uncertainty in the calibration of the measurement system. The estimated nonlinear coefficient

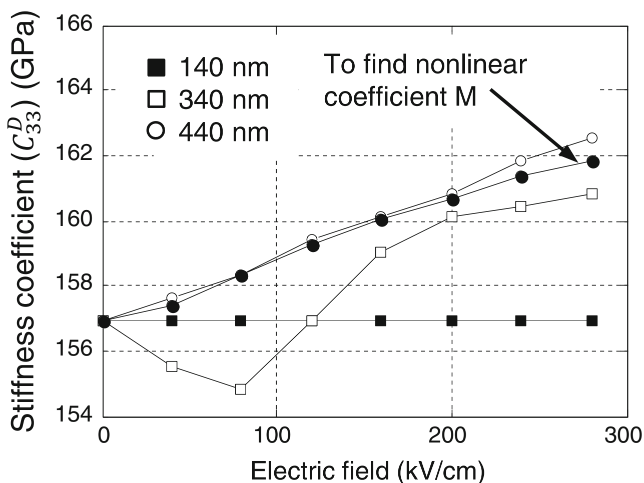

Fig. 11 Stiffness coefficient (**a**) and coupling coefficient (**b**) of PZT thin films as a function of electric field

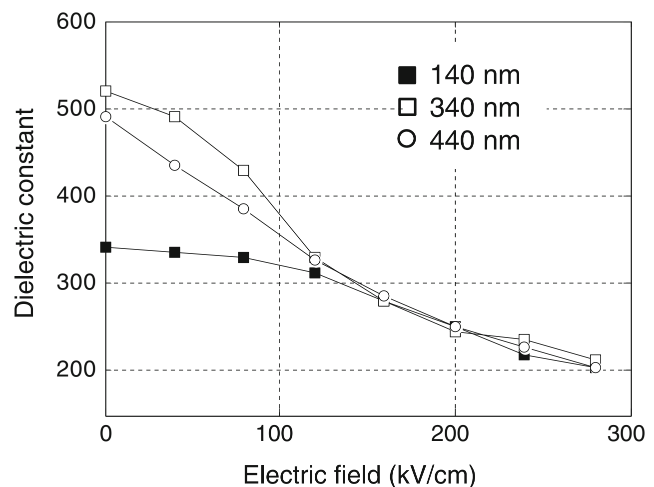

Fig. 13 Dielectric constants for various PZT thin film thicknesses as a function of DC electric field

(M) of the electrostriction using (15) was ~1.9×10^{19} Nm^2/C^2 for a 440 nm thick PZT film.

$$c_{33}^D = c_o^D + M\left(\varepsilon_r^S \varepsilon_o E_{DC}\right)^2 [30] \qquad (15)$$

Figure 12 shows that the electromechanical coupling coefficient (K_t^2) of PZT films calculated using Eq. (13) is thickness dependent and DC electric field dependent. The K_t^2 value is larger than 10% at 160 kV/cm for the 340 nm and 440 nm PZT films. Figure 13 shows the dielectric constants of PZT thin films as a function of DC electric field obtained in the simulation of the acoustic properties. It is seen that after 100 kV/cm, the dielectric constants become close to each other as seen in Fig. 7.

4 Conclusions

In this report, the microwave dielectric properties of PZT thin films deposited onto Pt using the CSD method were studied for RF applications. The measurements showed that the extracted dielectric constants of PZT thin films exceeded 540 and 280 for thicknesses of 440 nm and 140 nm, respectively, at 4 GHz. The large dielectric constant and moderate loss tangent (<1% at 4 GHz) suggest that PZT thin films may be suitable for use in RF applications such as high density MIM capacitors. The thin films may also be applicable in RF tunable devices requiring high tunability. The acoustic resonance analyses with DC bias voltages for the multilayer capacitor structure with PZT thin films demonstrate that the simulation results were in strong agreement with the experimental measurements and also show the possibility of a DC electric field dependent tuning of the PZT thin films. The resonant frequency shift was ~15 MHz. It was shown that the microwave measurements performed using the MIM capacitor structures fitted with an annular ring slot on the top of the metal layer enabled various measurements in one test wafer.

Acknowledgement The authors wish to acknowledge the assistance and support of SINTEF ICT and SINTEF Materials and Chemistry, Oslo and Juyeon Lee in cooperative center for research facilities, SKKU, Korea. This work is partially funded by the Norwegian Research Council under Grant No. 181712/I30 “Microtechnological Research Platform”.

References

1. R.G. Polcawich, J.S. Pulskamp, D. Judy, P. Ranade, S. Trolier-McKinstry, M. Dubey, IEEE Trans. Microw. Theor. Tech. **55**, 2642 (2007)
2. J. Conde, P. Muralt, IEEE Trans. Ultrason. Ferroelectr. Freq. Control. **55**, 1373 (2008)
3. N.F.M. Lazim, Z. Awang, Z.A. Majid, A. Yusof, A. Dollah, Asia-Pac. Confer. Appl. Electromagn. (APACE-2007) **484** (2007)
4. G. Arlt, U. BGttger, S. Witte, Appl. Phys. Lett. **63**, 602 (1993)
5. J. Hector, N. Floquet, J.C. Niepce, P. Gaucher, J.P. Ganne, Microelectron. Eng. **29**, 285 (1995)
6. R.J. Ong, D.A. Payne, N.R. Sottos, J. Am. Ceram. Soc. **88**, 2839 (2005)
7. S.E. Moon, E.K. Kim, S.J. Lee, M.H. Kwak, Y.T. Kim, H.C. Ryu, W.J. Kim, T.K. Song, J. Electroceram. **13**, 257 (2004)
8. X.G. Tang, L.L. Jiang, A.L. Ding, Microelectron. Eng. **65**, 387 (2003)
9. L. Lian, N.R. Sottos, J. Appl. Phys. **87**, 3941 (2000)
10. G.T. Park, C.S. Park, J.J. Choi, J.W. Lee, H.E. Kim, J. Am. Ceram. Soc. **89**, 2314 (2006)
11. P.K. Singh, R.S. Cochrane, J.M. Borrego, E.J. Rymaszewski, T.M. Lu, K. Chen, IEEE MTT-S Intern. Microw. Sympo. Digest. **3**, 1457 (1994)
12. K. Ikuta, Y. Umeda, Y. Ishii, Jpn. J. Appl. Phys. Part 2 Lett. **34**, L1211 (1995)
13. Z.X. Ma, A.J. Becker, P. Polakos, H. Huggins, J. Pastalan, H. Wu, K. Watts, Y.H. Wong, P. Mankiewich, IEEE Trans Electron Dev **45**, 1811 (1998)
14. D. Min, N. Hoivik, G.U. Jensen, F. Tyholdt, U. Hanke, J. Phys. Appl. Phys. **44**, 255404 (2011)
15. P. Rundqvist, A. Vorobiev, S. Gevorgian, K. Khamchane, Integr. Ferroelectr. **60**, 1 (2004)
16. F. Tyholdt, F. Calame, K. Prume, H. Raeder, P. Muralt, J. Electroceram. **19**, 311 (2007)
17. M.K. Kazimierczuk, *High-frequency magnetic components*, 1st edn. (Wiley, 2009), pp. 98–111
18. D.Y. Chen, J.D. Phillips, J. Electroceram. **17**, 613 (2006)
19. S. Gevorgian, A. Vorobiev, T. Lewin, J. Appl. Phys. **99** (2006)
20. N. Delmonte, B.E. Watts, G. Chiorboli, P. Cova, R. Menozzi, Microelectron. Reliab. **47**, 682–685 (2007)
21. X.N. Zhu, V. Lee, J. Phillips, A. Mortazawi, IEEE Microw Wireless Compon Lett **19**, 359 (2009)
22. G. Suchaneck, W.M. Lin, R. Koehler, T. Sandner, G. Gerlach, R. Krawietz, W. Pompe, A. Deineka, L. Jastrabik, Vacuum **66**, 473 (2002)
23. C.R. Cho, L.F. Francis, J. Mater. Sci. Lett. **19**, 1477 (2000)
24. P.K. Larsen, G.J.M. Dormans, D.J. Taylor, P.J.J. Vanveldhoven, Appl. Phys. **76**, 2405 (1994)
25. M.J. Liu, H.K. Kim, J.J. Blachere, Appl. Phys. **91**, 5985 (2002)
26. C. Zinck, E. Defay, A. Volatier, G. Caruyer, D.P. Tanor, L. Figuiere, 14th IEEE Int. Symp. Appl. Ferroelectrics (ISAF-04) **29** (2004)
27. K.M. Lakin, G.R. Kline, K.T. McCarron, IEEE Trans Microw Theor Tech **41**, 2139 (1993)
28. A.L. Kholkin, E.L. Colla, A.K. Tagantsev, D.V. Taylor, N. Setter, Appl. Phys. Lett. **68**, 2577 (1996)
29. Q.X. Su, P. Kirby, E. Komuro, M. Imura, Q. Zhang, R. Whatmore, IEEE Trans Microw Theor Tech **49**, 769 (2001)
30. S. Sanchez, G. Le Rhun, A. Suhm, E. Defay, European Microw. Confer (EuMC) **799** (2010)